JGR Oceans

RESEARCH ARTICLE
10.1029/2023JC019715

Modulation of Western South Atlantic Marine Heatwaves by Meridional Ocean Heat Transport

Marlos Goes[1,2], Shenfu Dong[2], Gregory R. Foltz[2], Gustavo Goni[2], Denis L. Volkov[1,2], and Ilana Wainer[3]

[1]Cooperative Institute for Marine and Atmospheric Studies, University of Miami, Coral Gables, FL, USA, [2]Atlantic Oceanographic and Meteorological Laboratory, NOAA, Miami, FL, USA, [3]Oceanographic Institute, University of São Paulo, São Paulo, Brazil

Key Points:

- Marine heatwaves and cold spells are in phase with westward propagating sea level anomaly features
- Meridional advection is important for the interannual mixed layer heat budget in the western South Atlantic
- The South Atlantic Meridional Overturning Circulation leads the beginning of the westward-propagating sea level mode by 3–9 months

Supporting Information:

Supporting Information may be found in the online version of this article.

Correspondence to:

M. Goes,
marlos.goes@noaa.gov

Citation:

Goes, M., Dong, S., Foltz, G. R., Goni, G., Volkov, D. L., & Wainer, I. (2024). Modulation of western South Atlantic marine heatwaves by meridional ocean heat transport. *Journal of Geophysical Research: Oceans*, *129*, e2023JC019715. https://doi.org/10.1029/2023JC019715

Received 3 FEB 2023
Accepted 22 JAN 2024

Author Contributions:

Conceptualization: Marlos Goes, Shenfu Dong, Gregory R. Foltz, Gustavo Goni, Denis L. Volkov, Ilana Wainer
Data curation: Shenfu Dong
Formal analysis: Marlos Goes
Funding acquisition: Marlos Goes, Gustavo Goni, Denis L. Volkov
Investigation: Marlos Goes
Methodology: Marlos Goes, Shenfu Dong, Gregory R. Foltz, Denis L. Volkov
Resources: Shenfu Dong
Software: Marlos Goes, Gregory R. Foltz
Validation: Marlos Goes
Visualization: Marlos Goes
Writing – original draft: Marlos Goes

Abstract Marine heatwaves and cold spells are extreme surface temperature events that have been associated with adverse societal and ecosystem impacts in several regions around the globe. Predicting these events presents a challenge because of their generally short-lived nature and dependence on air-sea interactions, both locally and remotely. Here we analyze oceanic propagating features that promote the occurrence of marine heatwaves and cold spells in the western subtropical South Atlantic. The main interannual feature detected from satellite sea level data since 1993 shows a westward propagating zonal pattern with a periodicity of 3–5 years. The pattern has a significant in-phase correlation with sea surface temperature (SST) anomalies in the western South Atlantic, explaining 82% of the daily extreme warm (90th percentile) and cold (10th percentile) SST anomalies and consequently modulating interannual variations in the intensity and duration of marine heatwave and cold spell events. It is found that meridional oceanic advection plays an important role in the regional heat budget associated with the westward-propagating mode, modulating the meridional exchange of tropical (warm) and extratropical (cold) waters in the western subtropical South Atlantic region and thereby setting a baseline for temperature extremes on interannual timescales. This propagating mode is well correlated ($r > 0.6$) with the strength of the meridional overturning circulation at 25°S and 30°S with a lag of approximately 3–9 months. The lagged response provides a potential source of predictability of extreme events in the western South Atlantic.

Plain Language Summary Here we show that ocean dynamics can affect marine heatwaves (MHWs) and cold spells (CSs) in the western subtropical South Atlantic. We focused our analysis on the sea level anomaly features that propagate westward, crossing the basin in 3–5 years near 30°S. As they propagate, the sea level anomalies drive clockwise (for negative anomalies) or anticlockwise (for positive anomalies) ocean circulation around them. The circulation transports either tropical or subpolar waters into the subtropical region, warming and cooling the subtropical region, respectively, and influencing MHWs and CSs. Since the anomalies influence meridional ocean transport, we analyzed their link to the basin integrated meridional heat transport associated with the Atlantic Meridional Overturning Circulation. We show that there is a good correlation between the phase of the sea level and circulation anomaly propagation (either centered in the eastern, western or interior of the basin) and the meridional heat transport. Therefore, the South Atlantic Meridional Overturning Circulation index can serve as an early warning of MHWs and CSs in the subtropical western South Atlantic.

1. Introduction

Marine heatwaves (MHWs) and cold spells (CSs) are sustained extreme warm and cold sea surface temperature (SST) anomalies, respectively. In particular, MHWs have received considerable attention in recent years, but both MHWs and CSs can have drastic impacts on marine ecosystems (e.g., Schlegel et al., 2021), such as coral bleaching (Couch et al., 2017; Dalton et al., 2020; Hsieh et al., 2008; Le Nohaïc et al., 2017; Zapata et al., 2011), changes in primary productivity and hypoxia (Sen Gupta et al., 2020; Wheeler et al., 2003), pelagic species mortality (McEachron et al., 1994; Smale et al., 2019; Woodhead, 1964), and closing of commercial and recreational fisheries (Cavole et al., 2016; Chang et al., 2013; Santos et al., 2016; Stuart-Smith et al., 2018). The compound effect of extreme temperatures with other stressors such as ocean acidification, tropical cyclones, algae blooms, and marine pollution, can have long-term impacts on marine ecosystems. In addition to these stressors, global warming affects the baseline of transient anomalies (Hobday et al., 2018) and, therefore, there has been an

Writing – review & editing: Marlos Goes, Shenfu Dong, Gregory R. Foltz, Gustavo Goni, Denis L. Volkov, Ilana Wainer

increase in the duration, frequency and intensity of MHWs relative to CSs in most regions of the globe (Costa & Rodrigues, 2021; Frölicher & Laufkötter, 2018; Oliver et al., 2018).

One of the most resilient MHW events was registered in the Northeast Pacific region during 2013–2016. This event, commonly known as the "Blob," has been linked to large scale atmospheric and oceanic patterns such as a reduction in wind-driven upper-ocean mixing and a shallow mixed layer depth (Amaya et al., 2020; Di Lorenzo & Mantua, 2016; Joh & Di Lorenzo, 2017). Other recent studies have shown the importance of the ocean state for similar types of extreme temperature anomalies in different basins. For instance, the occurrence, location and intensity of MHWs in the Tasman Sea have been linked to upper 2,000 m warm ocean heat content anomalies on interannual to decadal timescales (Behrens et al., 2019), and the likelihood of MHWs near the East Australian Current has been shown to be modulated by westward propagation of Rossby waves (Li et al., 2020).

In the western South Atlantic, Rodrigues et al. (2019); Li et al., 2020 linked the occurrence of MHWs to blocking events associated with atmospheric Rossby wave trains propagating from the South Pacific Ocean. These blocking events are characterized by increased atmospheric sea level pressure, suppressed formation of clouds and increased solar radiation into the ocean. For some MHW events, this mechanism can be the trigger. In another study, Manta et al. (2018) found that the year of 2017 was also characterized by an intense MHW over the continental shelf off the Rio da Plata in Uruguay, and this event was triggered by extreme atmospheric heat fluxes related to reduced winds. However, the large-scale ocean circulation may precondition or interact with these events and, thus, modulate their occurrence on interannual timescales. For example, Goes et al. (2019) showed that the South Atlantic MHW during the austral summer of 2009/2010 propagated zonally from the center of the basin to the east coast of South America near 22°S. Upon reaching the western boundary, this MHW propagated southwards along the Brazil Current and dissipated two months later near 30°S. The mechanisms by which large-scale ocean processes may influence MHW events in the South Atlantic are mostly unknown. In other locations, such as the North Atlantic, the tripole pattern, which is the first mode of interannual variability of SST and sea level anomaly (SLA), has been linked to convergences and divergences of the integrated meridional heat transport, which impacts the large scale upper ocean heat content and coastal sea level in neighboring areas (e.g., Roberts et al., 2016; Volkov et al., 2019).

In the South Atlantic, evidence has been found that large scale SST patterns can serve as a fingerprint for South Atlantic Meridional Overturning Circulation (AMOC) variability (Dima & Lohmann, 2010; Lopez et al., 2016), which may change the baseline for the occurrence of MHW and CS events in the region. This paper analyzes the effect of basin-scale propagating ocean anomalies on the occurrence of MHWs and CSs in the western South Atlantic. Known methodologies (Section 2.2) are used to detect the propagating modes and the extreme temperature events. A mixed layer heat budget analysis is presented to investigate the role of ocean advection and heat fluxes in the western South Atlantic (Section 3.3). Finally, a reconstruction of the AMOC in the South Atlantic will be used to infer the role of large-scale volume and heat transport in triggering these anomalies (Section 3.4). The implications of the results and the potential to predict extreme temperature events in the western South Atlantic is also discussed (Section 4).

2. Data and Methods

2.1. Data

Five main data sets are used in this work, consisting of SST and sea level height from remote sensing, reanalyses for the ocean (ORAS5) and air-sea interface (ERA5), and an AMOC reconstruction from satellite altimetry and in situ temperature.

The analysis of SST data is performed using the NOAA Optimum Interpolation Sea Surface Temperature data set (OISSTv.2; Reynolds et al., 2007), a blended global gridded product available daily at a 1/4° horizontal resolution since January 1982. Daily resolution is used to identify metrics of MHWs and CSs, and monthly resolution is used in basin-scale correlation maps. For the purpose of this work, the SST data are spatially regridded using a bilinear interpolation to a 1° × 1° horizontal resolution from 1993 to 2020.

The sea level analysis is performed using the monthly maps of sea level anomaly (SLA) from 1993 to 2020 processed and distributed by the Copernicus Marine Environment Monitoring Service (CMEMS). The SLA maps are produced on a 1/4° grid (Taburet et al., 2019) by merging data from all altimetry satellites available at a given time (Pujol et al., 2016). The SLA data at each grid point is computed with respect to a twenty-year (1993–2012)

mean. The seasonal cycle in SLA and all other variables is removed by subtracting the climatological monthly means computed for the whole analyzed period (~28 years for all variables).

Surface atmospheric variables used in this study come from the European Centre for Medium-Range Weather Forecasts' (ECMWF) ERA5 Reanalysis (Hersbach et al., 2020), which is distributed in a regular 0.25° horizontal grid. We use monthly fields of zonal and meridional wind, sea level pressure (SLP), and surface heat fluxes (shortwave, longwave, latent and sensible), regridded to a 1° × 1° horizontal grid from 1993 to 2020.

The monthly AMOC strength and meridional heat transport timeseries at four different latitudes in the South Atlantic (35°S, 30°S, 25°S, and 20°S) for the period 1993–2021 were produced using synthetic temperature profiles based on statistical relationships between SLA and the depths of isotherms (Dong et al., 2015, 2021), salinity profiles from historical T/S relationships (Goes et al., 2018), and monthly surface wind stress data from ERA5 for the Ekman component. The methodology has been validated against the AMOC and meridional heat transport estimates based on cross-basin expendable bathythermograph (XBT) high-density transect data near 35° S (Dong et al., 2015).

We examine vertical temperature anomalies and calculate the heat budget in the western South Atlantic using the ORAS5 reanalysis (Zuo et al., 2018), which is based on an ensemble of global eddy-permitting (0.25°) ocean model runs, forced with air-sea fluxes from ERA-Interim (1979–2015) and ECMWF NWP thereafter. The monthly output of ORAS5 is interpolated to a 1 × 1° horizontal grid and 75 vertical levels. For this work, we use the following ORAS5 fields: temperature (T), horizontal velocity (v), mixed layer depth (h), wind stress (τ) and net surface heat flux (Qnet) from 1993 to 2021.

2.2. Methods

2.2.1. Complex EOF

To define the interannual propagating patterns of SLA in the South Atlantic, first the monthly de-seasoned SLA fields are filtered using a bandpass wavelet filter of 0.8–16 years. Then we perform a Complex Empirical Orthogonal function (CEOF) analysis (e.g., Navarra & Simoncini, 2010; Rasmusson et al., 1981) to extract the main propagating patterns of variability between 15°S and 40°S. The CEOF uses a principal component analysis on a Hilbert (quadrature) transform of a field. Therefore, it produces real and imaginary parts of loadings (maps), here defined as $\mathrm{CEOF}_j(x,y)$ for a particular mode j, and their associated expansion coefficients or principal components ($\mathrm{PC}_j(t)$). The CEOFs and PCs are used to compute spatial and temporal amplitudes and phases, necessary conditions to describe a propagating wave pattern (Majumder et al., 2019). Therefore, the advantage of using CEOFs is the ability to define a propagating mode in space and time, as opposed to conventional EOFs which only provide snapshots of two phases (0° or 180°) of the propagation (Rasmusson et al., 1981). The SLA, associated with a particular mode of the variability j ($\mathrm{SLA_j}$), can be reconstructed as the product of its loadings and its associated expansion coefficients:

$$\mathrm{SLA}j(x,y,t) = \mathrm{PC}_j(t) \times \mathrm{CEOF}_j(x,y). \quad (1)$$

The time evolution of the mode j can be examined by rotating in phase the CEOF and the PC by an angle θ using a rotation matrix $R_{2x2}(\theta)$, which produces the same reconstruction:

$$\mathrm{SLA}j(x,y,t) = R(\theta) \cdot \mathrm{PC}_j(t) \times R(\theta) \cdot \mathrm{CEOF}_j(x,y) \quad (2)$$

Cross-correlations and composites of SST, SLP, and 10-m wind anomalies are obtained for the rotated phases of the CEOF modes, using a 13-month Gaussian filter on these variables to remove sub-annual timescales.

2.2.2. Definition of Marine Heatwaves and Cold Spells

The MHWs and CSs are defined as the extreme SST anomaly (SSTA) events that are above the seasonally varying the 90th percentile and below the 10th percentile, respectively, and last for at least 5 days (Hobday et al., 2016). We follow the definitions of MHWs and CSs described in Hobday et al. (2016) using detrended daily values of SSTA at a 1° × 1° degree horizontal resolution. The K-means cluster analysis (Arthur & Vassilvitskii, 2007), which is a method that minimizes the Euclidean distance between groups of observations, is used to determine the

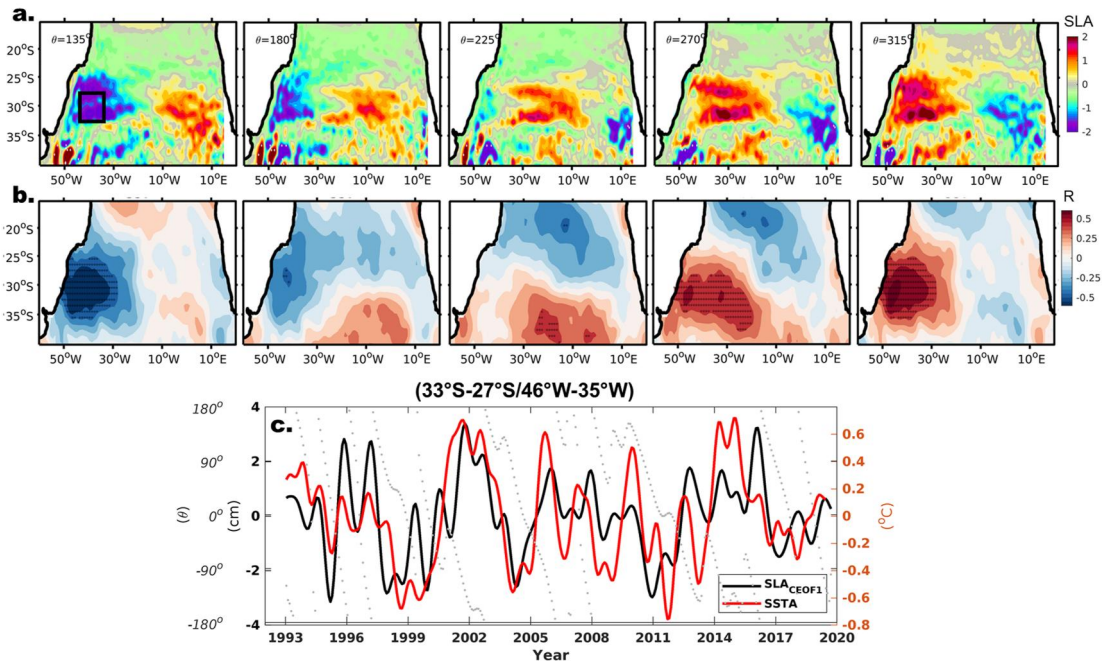

Figure 1. (a) SLA spatial phase (cm) of the first interannual CEOF mode at 45° phase snapshots. (b) Correlation of SST anomalies from 1993 to 2020 with the PC1 timeseries for the respective temporal phases shown on top. SST anomalies were previously low-passed with a 13-month Gaussian filter. Hatched regions show the statistically significant regions according to a double tailed Student *t*-test method. (c) Timeseries of SST anomalies (red) and SLA reconstructed by the CEOF1 (black) averaged between 33°S and 27°S/46°W and 35°W (black box in top left panel). Dots are the temporal phase (in degrees) from the CEOF mode.

large-scale SSTA patterns associated with MHWs or CSs events. The cluster analysis is a method of dimension reduction, therefore categorizing the sparse extreme SSTA events into a set of spatial and temporal modes. In this analysis, we identified the locations where the daily SST anomalies crossed the MHW and CS thresholds and divided them into four clusters. The method was applied to MHW and CS anomalies separately, and then we visually selected the cluster modes that were mostly related to the western subtropical South Atlantic region.

2.2.3. Mixed Layer Heat Budget

To examine the roles of atmospheric and oceanic contributions to the mixed layer temperature changes, we use a simplified temperature tendency equation:

$$\underbrace{\frac{\partial T}{\partial t}}_{(a)} = \underbrace{\frac{(Q_{net} - Q_{pen})}{\rho_0 C_p h}}_{(b)} - \underbrace{v \cdot \nabla_H T}_{(c)} - \underbrace{w \frac{\Delta T}{h}}_{(d)} + \underbrace{R}_{(e)}, \quad (3)$$

which states that the mixed layer temperature tendency (*a*) is driven by contributions from the net surface heat flux (*b*), horizontal advection (*c*), and vertical entrainment (*d*). The residual *R* (*e*) represents unresolved processes such as horizontal and vertical mixing, eddy covariances, and the accumulation of errors from the terms (*a*)–(*d*) (Vialard et al., 2001). The mixed layer depth (*h*) provided by the reanalysis is calculated using the criterion of an increase in potential density of 0.03 kg·m^{-3} from the surface. Mixed layer depth typically varies from 15 to 180 m in the western South Atlantic. Temperature (*T*) and horizontal velocity (*v*) are averaged over the mixed layer. In (*b*), *Q*net is reduced by the amount of shortwave radiation that penetrates through the base of the mixed layer (Q_{pen}), estimated from an exponential function of surface ocean color (Morel & Antoine, 1994; Sweeney et al., 2005). Shortwave radiation from ERA5 is used in the Q_{pen} calculation, since ORAS5 does not provide shortwave radiation as a standard output. In addition, ocean color is derived from the SeaWiFS satellite climatological Chlorophyll-a concentration data, interpolated from its original 9 km resolution to the ORAS5 output grid. In the entrainment term (*d*), ΔT is the difference between the mixed layer temperature and the temperature

5 m below the mixed layer and w is the entrainment velocity at the base of the mixed layer (upward only, given by the Heaviside function: $H(w > 0) = 1$; $H(w < 0) = 0$), estimated as:

$$w = H\left(w_h + \frac{\partial h}{\partial t} + v \cdot \nabla h\right), \tag{4}$$

which consists of a mass flux that crosses an isopycnal surface (Stevenson & Niiler, 1983). The vertical entrainment velocity is decomposed into vertical advection or the Ekman pumping contribution ($w_h = \nabla \times \left(\frac{\tau}{\rho_0 f}\right)$), the tendency of the mixed layer ($\partial h/\partial t$), and the horizontal induction across the mixed layer ($v \cdot \nabla h$). The constants used are the density of seawater ($\rho_o = 1{,}025$ kg m^{-3}) and the specific heat of seawater ($C_p = 4{,}000$ J kg^{-1} K^{-1}).

The horizontal advection term (c) can be further decomposed into its mean (bar) and time-variable (prime) constituents:

$$uT_x + vT_y \approx u'\overline{T_x} + v'\overline{T_y} + \overline{u}T_x' + \overline{v}T_y', \tag{5}$$

where the subscripts denote the gradient in the x and y directions, the mean variability is defined as a 28-year mean, and the time-variable component is the residual from the mean. In the analysis of interannual variability of heat budget and heat transport, a 19-month window is applied to better match the variability of the PC.

3. Results

3.1. The Main Propagating Mode in the South Atlantic

The main propagating mode of SLA at interannual timescales in the South Atlantic (CEOF1) is an east-west pattern centered between 25°S and 35°S (e.g., Majumder et al., 2019). This mode has a main periodicity of 3–5 years and explains ∼28% of the interannual variance of SLA in the South Atlantic (Figure 1c). The correlation between the reconstructed SLA and the band-pass filtered SLA reaches $r = 0.75$, and the correlation with SSTA reaches $r = 0.7$, averaged over 33°S–27°S and 46°W–35°W in the western subtropical South Atlantic (Figure 1c). The evolution of this pattern for half-cycle (0–180° phase) snapshots every 45° (Figure 1a) shows that it has a signature in the South Atlantic SST field (Figure 1b), in that the correlation of SSTA with this mode shows an in-phase relationship pattern, where positive (negative) SLA are associated with high (low) SSTA. These co-located in-phase SLA and SSTA are observed mostly in the eastern and western parts of the basin. In the center of the basin, the anomalies in sea level and SST do not overlap; instead the SST correlation map shows a dipole pattern centered at ∼30°S, which hints at an exchange of waters from north and south of the region. This SST dipole pattern is similar to the South Atlantic Subtropical Dipole mode (SASD), which is the leading EOF mode of interannual SST variability in the South Atlantic, explaining about 24% of the total variance (e.g., Morioka et al., 2011; Wainer et al., 2014). The SASD mode has been previously correlated to EOFs of the east-west SLA mode (Grodsky & Carton, 2006), suggesting a connection between the tropics and subtropics via Kelvin and Rossby waves. The SASD variability has been associated with changes in the strength of the subtropical high, which interacts with SST by changing the wind speed pattern and latent heat flux (Sterl & Hazeleger, 2003).

The vertical structure of temperature anomalies and their association with the propagating SLA features are shown in Figure 2. The longitude-time diagram of the upper 500 m temperature anomalies (T500) from ORAS5 reanalysis and SLA (Figure 2a), averaged between 32°S and 28°S, shows that T500 propagates along with the SLA from east to west in approximately 5 years. The vertical structure of these temperature anomalies in two different longitudinal areas, [15–20]°W and [35–40]°W (Figures 2b and 2c), shows that they are generally subsurface intensified and located mostly in the upper 200 m near the base of the mixed layer. This association suggests that SST anomalies are linked to ocean dynamics and heat transport.

3.2. Detection of Marine Heatwaves and Cold Spells

Given the in-phase relationship found between the propagating SLA and SST signals in the South Atlantic, in this section we investigate whether this mechanism can serve as a precursor for the frequency and duration of extreme daily near-surface temperature. We apply a cluster analysis to the SSTA during the MHW/CS events, calculated

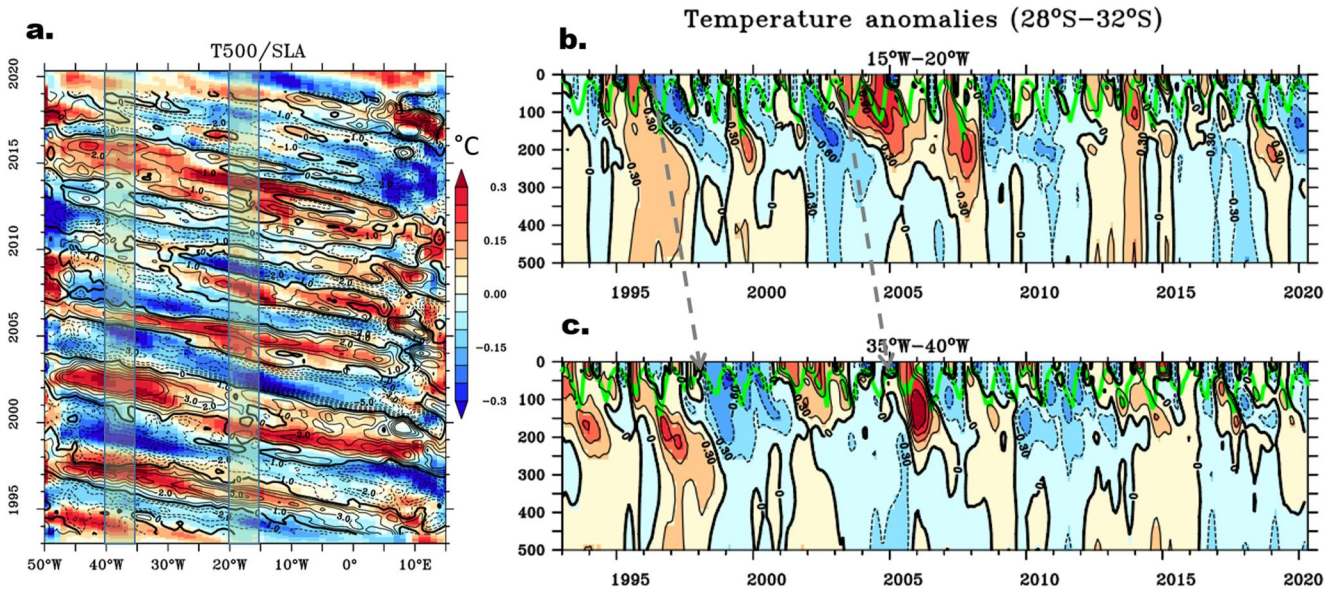

Figure 2. (a) Longitude-time evolution of the monthly temperature anomalies from ORAS5 reanalysis averaged between 28 and 32°S and over the upper 500 m (shaded) overlaid by monthly SLA in meters (black contours). Data was detrended, the zonal means were subtracted to show the propagating features, and a 13-month triangular filter was applied to highlight the interannual variability. Time-depth evolution of detrended ORAS5 temperature anomalies averaged between 28 and 32°S and between the longitudinal ranges (highlighted by green shades in (a)) of (b) 15 and 20°W, and (c) 35 and 40°W. The green line in (b) and (c) represents the MLD. Dashed arrows between (b) and (c) highlight the inferred timescale of propagating features between the two longitudinal ranges.

on a 1° × 1° grid, to define the four main clusters of MHWs and CSs in the South Atlantic (Figure S1 in Supporting Information S1). The clusters in which centroids are located in the western South Atlantic are selected to be used as the MHW and CS modes (Figure 3). These modes show similar patterns: large-scale cooling (Figure 3a) and warming (Figure 3b) centered near [30°S, 30°W] with a maximum intensity of approximately 1.5° C. The temporal evolution of their occurrence and intensity shows year-to-year variability with a slight trend toward more frequent MHW events in recent years relative to CS, suggesting that non-linear SST trends may exist in the South Atlantic during the analyzed period.

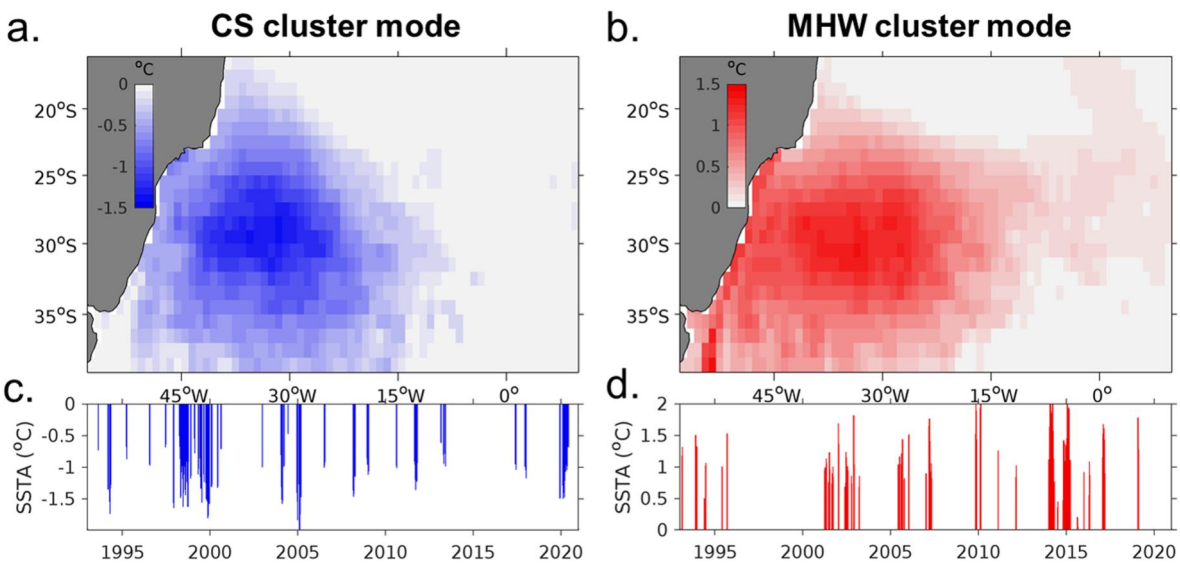

Figure 3. Marine (a, c) cold spell and (b, d) heatwave SST anomaly modes related to the western subtropical South Atlantic derived from a cluster analysis. Top panels (a, b) show the spatial maps of the anomalies and bottom panels (c, d) are the respective daily time series calculated from the averaged patterns on panels (a, b).

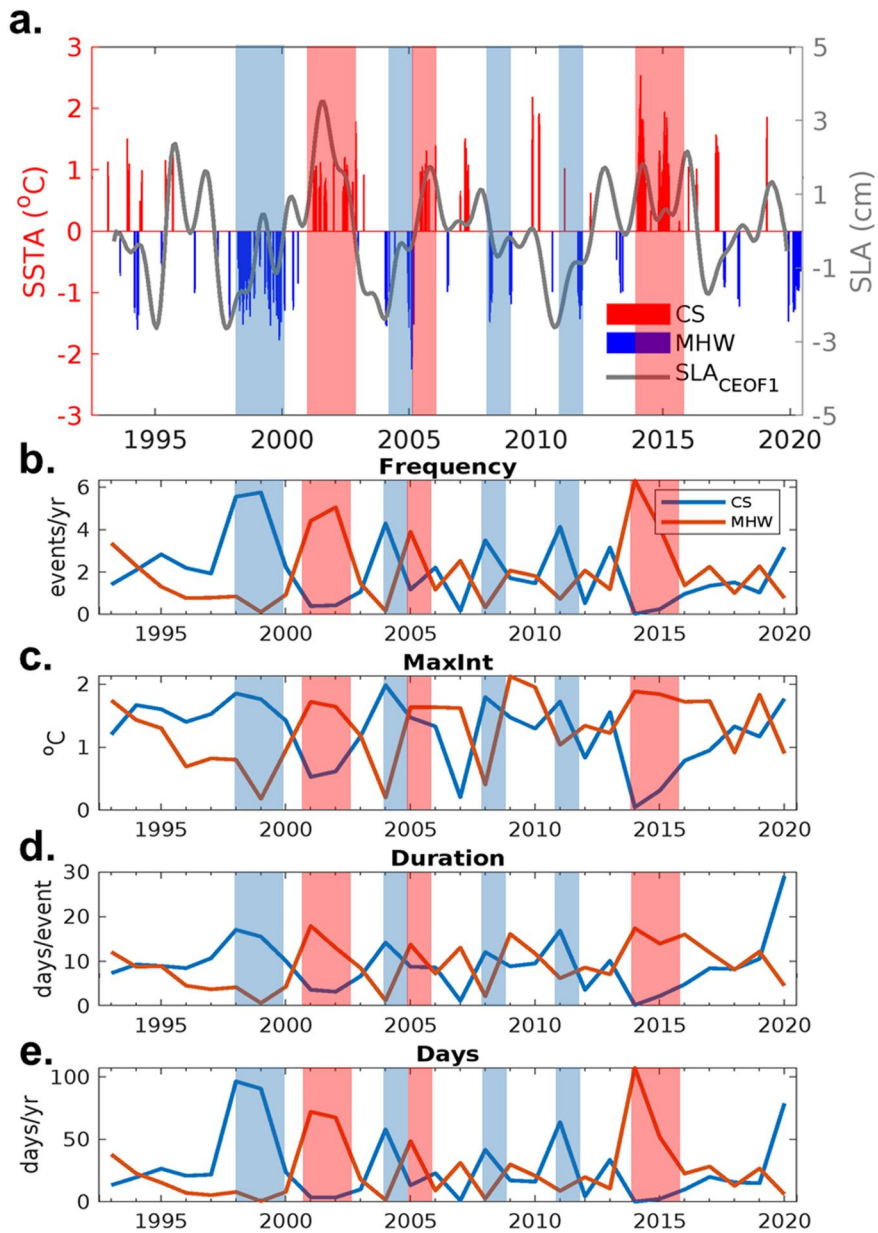

Figure 4. (a) Averaged daily SST anomalies (°C) associated to the western South Atlantic cluster mode of MHW (red bars) and CS (blue bars) overlaid by the time series of the SLA (gray line) in the western South Atlantic reconstructed from the CEOF1 mode. Annual averages of (b) Frequency, (c) Maximum Intensity (MaxInt), (d) Duration, and (e) Days per year of MHW (red) and CS (blue) in the western South Atlantic. The blue and shaded areas are selected years with strong CSs (1998, 1999, 2004, 2008, and 2011) and MHWs (2001, 2002, 2005, 2014, and 2015), respectively.

To understand the co-variability of the extreme SST events and the propagating SLA features, the joint variability of MHW and CS cluster modes of Figure 3 is compared with the reconstructed SLA from the CEOF1 mode in the western South Atlantic (Figure 4a). A clear correspondence between the extreme SST events and the propagating SLA mode is observed, in which daily warm SST extremes are associated with high SLA anomalies, and vice-versa. To quantify this relationship, a conditional probability is calculated. The probability of MHW and CS events conditional to the CEOF phase is calculated using the Bayes' theorem (Supporting Information S1). Four probabilities are examined, which are calculated from the combination of two binary variables, one associated with the sign of the CEOF1 SLA reconstruction (CEOF+, CEOF-) and the other to the occurrence of extreme daily SST events (MHW, CS). The estimated values of conditional probabilities (Figure S2 in Supporting

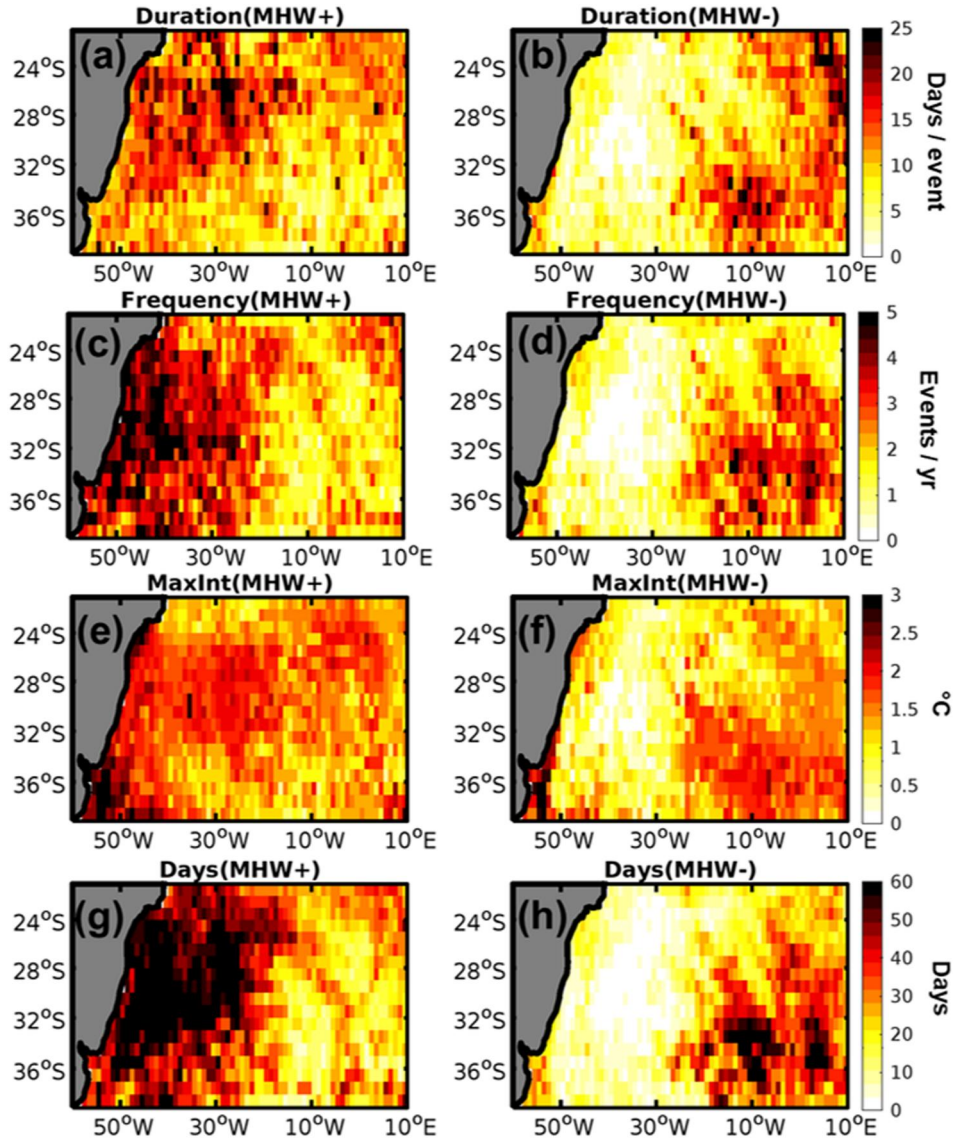

Figure 5. Composites of annual marine heatwave metrics for (left) years with high MHW occurrences (MHW+: years 2001, 2002, 2005, 2014, and 2015) and (right) for years with low MHW occurrences (MHW−: years 1998, 1999, 2004, 2008, and 2011). The MHW metrics are (a, b) duration, (c, d) frequency, (e, f) maximum intensity (maxInt), and (g,h) MHW days per year, calculated according to Hobday et al. (2016).

Information S1) suggest that the occurrence of extreme SST events and SLA with the same phase, that is, P(MHW | CEOF+) = 82.2% and P(CS | CEOF-) = 81.0%, are much more likely than the events with opposite phase, that is, P(MHW | CEOF-) = 19.0% and P(CS | CEOF+) = 17.8%. The total conditional probability that both MHW and CS events are in phase with the SLA reconstructed from the CEOF1 mode is calculated simply by averaging their two conditional probabilities, P(MHW | CEOF+) and P(CS | CEOF-), which results in ∼82% of the occurrences, suggesting a strong potential for using the propagating mode to predict such extreme events.

In further analysis, the annual metrics of the MHWs and CSs are analyzed (Figures 4b–4d). The time evolutions of the duration, frequency and intensity of the MHW and CS events averaged in the western South Atlantic often show out-of-phase relationships. The years with more intense, frequent and longer MHWs show weaker, less frequent and shorter CS events. Particular years that show such out-of-phase relationships are 2001, 2002, 2009, 2014, and 2015 for more positive (MHW) events, and 1998, 1999, 2004, 2008, and 2011 for more negative (CS) events. During those years with increased MHW occurrence there are approximately five to six events, with an

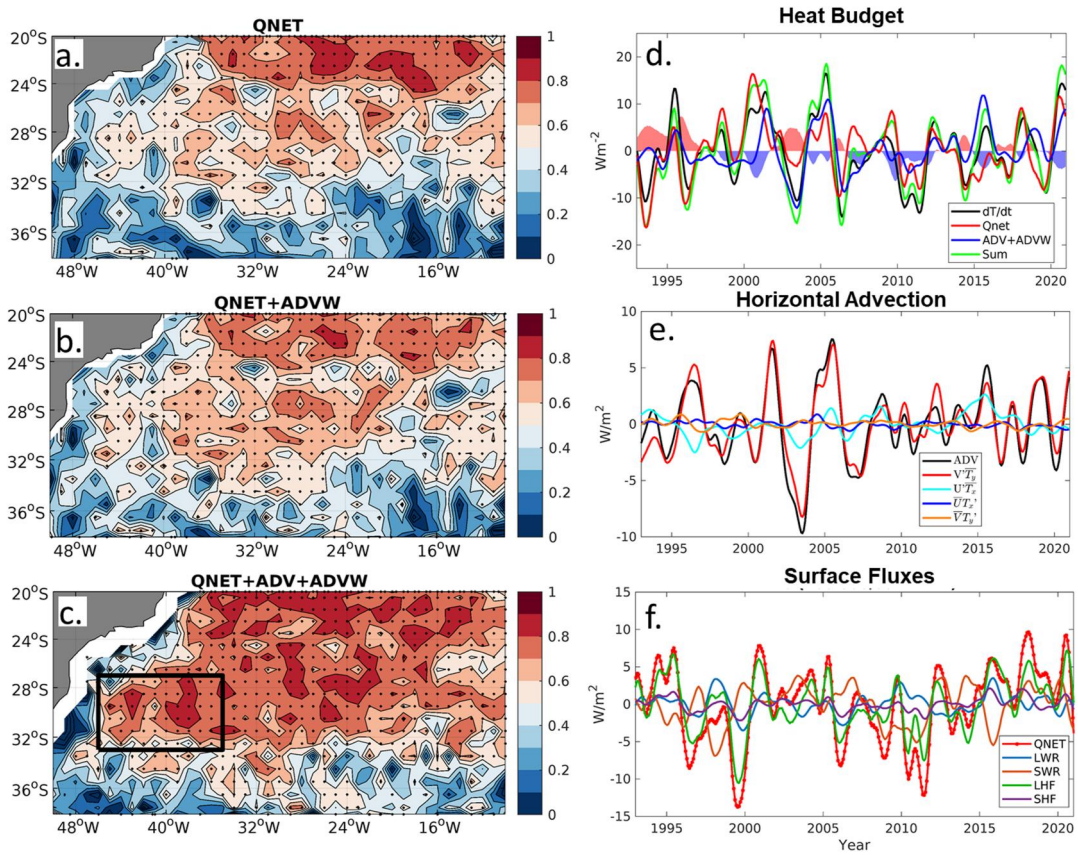

Figure 6. (a–c) Maps of correlation between the anomalies of temperature tendency (*dT*/*dt*) and the anomaly terms of the mixed heat budget: (a) *Q*net, (b) *Q*net + ADVW, and (c) *Q*net + ADVW + ADV. The black box in (c) represents the region where the heat budget timeseries were calculated (27–33°S/35–46°W). Hatched areas are the locations above 95% significance. (d) Mixed layer heat budget anomalies averaged in the box. Red/blue shading represent the residuals (*dT*/*dt* minus Sum). (e) ADV (black) and its decomposition into meridional (VTy) and zonal (UTx) directions divided into eddy and mean contributions (see Equation 5 in Section 2.2.3). (f) Timeseries of the components of the anomalous surface heat flux (*Q*net) from ERA5 reanalysis: latent (LHF), sensible (SHF), shortwave (SWR) and longwave (LWR) fluxes. The mixed layer budget terms are labeled mixed layer temperature tendency (*dT*/*dt*), surface fluxes (*Q*net), horizontal advection (ADV), vertical advection (ADVW) and Sum = QNET + ADV + ADVW. Anomalies are calculated by subtracting the monthly climatology of the monthly averages, and Gaussian low-pass filter of 19 months is applied to the timeseries.

intensity of 1.5–2°C and duration of 10–20 days per event, resulting in more than 60 MHW days each year. A composite analysis of the three MHW metrics for the selected years with increased and decreased MHWs (Figure 5) shows that both events are characterized by a dipole between the eastern and western sides of the basin. Similar patterns are observed for CSs (not shown). Such a pattern suggests an out-of-phase occurrence of SST extreme events between east and west, which can be related to the propagating SLA mode for those years.

3.3. Mixed Layer Heat Budget

Here, we explore the potential role of surface heat fluxes and ocean advection in modulating MHWs on interannual timescales, using data from the ORAS5 and ERA5 reanalyses. The mixed layer heat budget is performed in a box within the region of maximum warming in the western subtropical South Atlantic, defined as 35°–46°W/27°–33°S (Figure 6a). The seasonal cycle of the mixed layer heat budget (Figure S3a in Supporting Information S1) is dominated by the *Q*net term. *Q*net warms the ocean during summer (November–March), and dampens the ocean's cooling during winter (May–September). The advection term is small, and vertical advection cools the ocean during fall (March–June), a period in which the mixed layer depth increases from 20 to 180 m. To focus on interannual timescales, monthly anomalies of the heat budget terms (Equation 3) are calculated, and a low-pass filter of 19 months is applied. To understand the spatial contributions of the terms in the mixed layer heat budget, a correlation analysis was performed between $\partial T/\partial t$ and the three analyzed components (Figures 6a–6c) by adding the components sequentially at each grid point. The correlation between $\partial T/\partial t$ and *Q*net (Figure 6a) is high

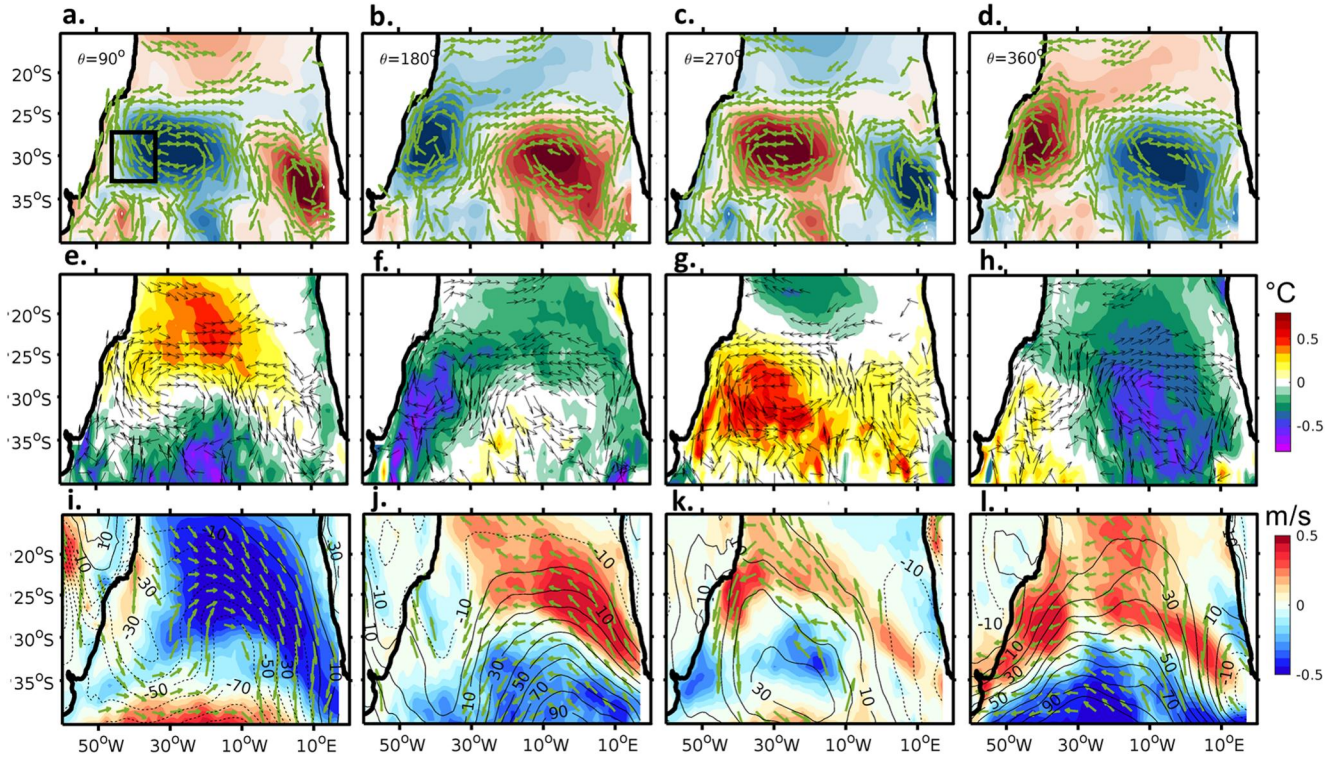

Figure 7. Composites for different phases of the propagating CEOF1 mode of SLA. Top panels: CEOF1 spatial pattern at 90° phases shown at the top left of panels a–d. The associated geostrophic current vectors are overlaid. The box of Figure 6 is shown in panel (a). Middle panels: Composites of SST anomalies (°C) with the geostrophic current vectors overlaid. Bottom panels: Composites of surface wind anomalies with the direction given by the arrows and speed (m/s) given by the shades. Overlaid on panels (i–l) are the contours of SLP anomalies (Pa).

($r > 0.7$) particularly in the tropical region north of 25°S, and more modest ($0.7 > r > 0.4$) in the subtropical region. Adding the vertical entrainment to Qnet does not increase the correlation values considerably, but some improvement is observed in the subtropical region. When horizontal advection is included, the correlations in the subtropical region north of 33°S increase almost everywhere, reaching values of $r = 0.9$ and above, which shows the importance of the oceanic contribution to changes in mixed layer temperature in the western South Atlantic.

The time evolution of the heat budget terms averaged in the western subtropical South Atlantic (box in Figure 6c) estimated in ORAS5 shows that the atmospheric (Qnet) and oceanic (horizontal advection and vertical entrainment) terms contribute similarly to the SST tendency (Figure 6d). The variability of the residual between the SST tendency and the sum of the atmospheric and oceanic contributions is smaller than the individual components, meaning that the residual does not have a major impact on the heat budget variability in the selected region. Other regions such as the western boundary and south of 35°S show lower correlations between changes in mixed layer temperature and the sum of atmospheric and oceanic terms (Figure 6c), probably due to eddy covariance and mixing terms.

On interannual timescales, the net surface heat flux from ERA5 is mostly dominated by the latent heat flux (Figure 6f) with a regression coefficient of 0.71, compared to much lower values for sensible (0.13), shortwave (0.07), and longwave (0.08) radiation components, and there is a good degree of compensation between shortwave and longwave + sensible radiative fluxes. Most of the contribution of the vertical entrainment term comes from the tendency of the mixed layer term ($\partial h/\partial t$), with smaller contributions from Ekman vertical advection and lateral induction terms (not shown). The decomposition of the horizontal advection term into meridional and zonal mean and time-variable components shows that $v'Ty$ is by far the dominant component (Figure 6e). This suggests that meridional velocity is driving the oceanic exchanges in the region. The dominance of the meridional component of temperature advection also holds for the seasonal variability (Figure S3b in Supporting Information S1) and emphasizes the importance of the Brazil Current transport for the mixed layer heat budget.

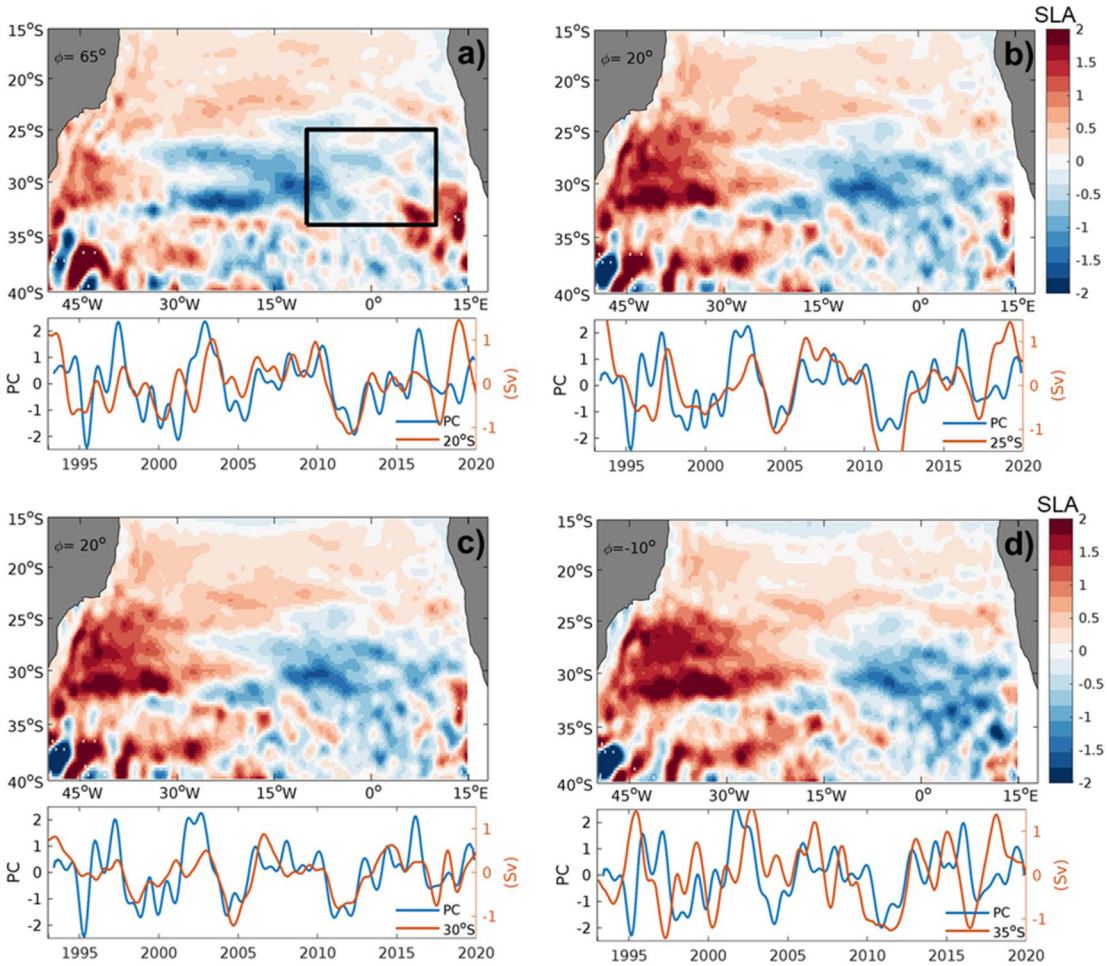

Figure 8. CEOF1 pattern of SLA in cm (maps) and PC1 and AMOC anomaly (timeseries) associated with the maximum correlation between PC1 mode and the AMOC anomalies at four different latitudes: (a) 20°S, (b) 25°S, (c) 30°S, and (d) 35°S. The maximum correlation between the AMOC and the CEOF1 is estimated by rotating the CEOF1 phase. The AMOC anomalies timeseries are given in Sv and smoothed with a 19-month Gaussian filter. The black box in (a) shows the region where the CEOF1 reconstructed SLA is used to calculate lagged correlations with the AMOC strength (Figure 9).

The results above suggest that the relationship between SLA and SST in the interior of the basin is mainly due to variations in advection and latent heat fluxes in the mixed layer (Figures 6d–6f). Using the SLA field for each phase of the propagating feature, we calculated the associated geostrophic velocities from the thermal wind relationship. For better visualization, the SLA was smoothed using a 5 × 5 degree Gaussian filter. According to geostrophy in the Southern Hemisphere, flow is cyclonic (clockwise) around a negative SLA, and anticyclonic (counterclockwise) circulation flows around a positive SLA (see Figure S4 in Supporting Information S1 for full propagation cycle). Therefore, a positive SLA anomaly would favor advection of warm tropical waters ahead of the westward propagating SLA, and cooler subpolar waters behind the SLA anomaly (Figures 7a–7d). Warm anomalies are then generally associated with southward advection and cold anomalies with northward advection. Consequently, the dipolar SST circulation centered over the SLA monopole anomaly (Figures 7e and g) is generated because of the exchange of waters between the subpolar and tropical regions that takes place in the subtropics. In addition, the CEOF1 mode is related to sea level pressure (SLP) anomalies in the center and south of the basin (Figures 7i–7l). SLP anomalies are collocated with SLA from the CEOF1 mode pattern at the center of the basin (90° and 270° phase angles) and have the same sign. A positive SLP anomaly (Figure 7k) may warm the surface locally due to a reduction of winds and cloud cover. It also generates an anticyclonic wind pattern around it, reinforcing the subtropical circulation and increasing the latent heat flux, particularly north of 30°S, thus contributing significantly to the dipole SST pattern. The opposite happens for the reverse phase (90°, Figure 7i). In the western side of the basin, strengthened winds may dampen the positive SSTA (Figures 7k and 7l), similar to what was shown in Sterl and Hazeleger (2003), leading to the transition to the next phase of the oscillation.

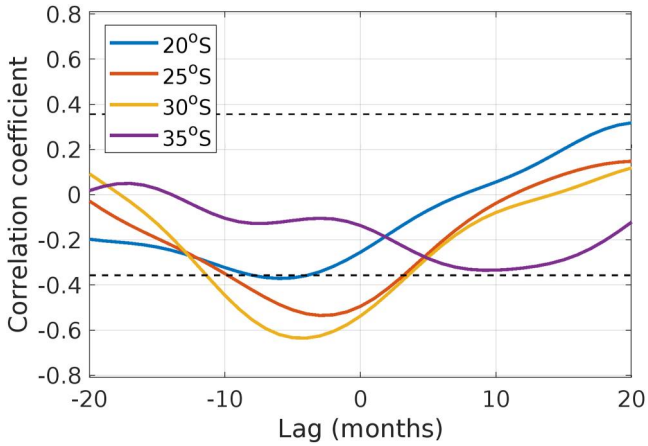

Figure 9. Lagged correlation of the reconstructed SLA in the eastern side of the basin (10°W–10°E/34°S–25°S; box in panel (a)) with the AMOC at four different latitudes (20°S, 25°S, 30°S, and 35°S) in the South Atlantic. For negative lags, the AMOC leads SLA. The dashed lines are the 90% confidence intervals given the adjusted degrees of freedom.

Composites of monthly SST, SLA, Wind speed, SLP, and MLD are also shown for four selected MHW (2002, 2014) and CS (1999, 2008) events (Figures S5 in Supporting Information S1). During the warm and cold events (Figure S5 in Supporting Information S1), the maximum intensity of SST anomalies is above 1°C. SSH anomalies of the same sign and magnitudes of up to 4 cm are observed in the western basin during these events. In general there are anomalies of the mixed layer of opposite sign relative to the SST, that is, shallower during warm events and deeper during cold events. The shallowing of the mixed layer is generally concomitant with a decrease in near-surface wind speed, and an anticyclonic (counterclockwise) wind anomaly pattern around a high SLP anomaly in the center-west of the basin. Therefore, the shoaling of the mixed layer under warm SST/SSH is a response to the reduction in wind speed and increases in stratification and buoyancy, which are mostly driven by horizontal advection and surface heat fluxes (Figure 6). Conversely, deepening of the mixed layer during cold events is associated with stronger, cyclonic winds, and weaker stratification.

3.4. Propagating SLA and AMOC

Volkov et al. (2019) showed that the tripole SLA pattern in the subtropical North Atlantic is partly driven by heat and freshwater divergence associated with the AMOC. Similarly, we investigate the link between the South Atlantic MOC at four different latitudes and the dominant SLA propagating feature. For this, we use the same methodology that was applied for generating Figure 1, in which the CEOF1 mode is rotated in phase (Equation 2). Similar to a lagged correlation, we calculate the correlation between the real part of PC1 and AMOC strength for each rotation angle θ, and select the angle at which the best correlation is achieved (Figure 8). This is performed with the AMOC time series at the four latitudes (20°S, 25°S, 30°S, and 34.5°S) computed by Dong et al. (2021). The AMOC time series agree reasonably well with PC1 at all analyzed latitudes, with correlations above 0.4. At 34.5°S, the phase relationship was not as clear in the beginning of the timeseries but improved after 2000. The weaker relationship may be due to the fact that the spatial pattern of the CEOF1 mode is more dominant north of 33°S. Indeed, Dong et al. (2021) showed that the AMOC at 34.5°S does not agree well with the AMOC at the other 3 latitudes further north. In addition, we can observe a slight shift toward the combination of higher angles and SLA patterns moving westward as the latitude at which the AMOC is calculated moves farther north (Figure 8), suggesting that coherent anomalies are advected from the south.

The lagged correlation between the AMOC and SLA reconstructed from CEOF1 mode in the eastern part of the basin (25°S–33°S/10°W–10°E) (Figure 9) shows that the magnitude of the correlation is largest at 30°S ($r = -0.63$, lag $= -4$; significant at 90%), followed by 25°S ($r = -0.56$, lag $= -3$), 20°S ($r = -0.43$, lag $= -5$), and 35°S ($r = -0.4$, lag $= 9$). The negative correlations indicate that when the AMOC is stronger, there is a negative sea level anomaly in the east and therefore a positive SLA in the western side of the basin. These correlations are mostly driven by the geostrophic component of the AMOC, with correlations of about 0.55 for 25°S and 30°S, with the Ekman component playing a smaller role. The typical lags are between 3 and 9 months, similar to the timescales of northward propagation defined in Dong et al. (2021). The negative lags suggest that the AMOC leads the propagating pattern and therefore could be a precursor to the propagation.

To further explore links between the propagating mode, the AMOC, and meridional heat transport (MHT), we calculated MHT using the reconstruction of Dong et al. (2021) across 30°S, the latitude with the highest correlation between CEOF1 and the AMOC. We divided the MHT across 30°S into western (west of 43°W), eastern (east of 3°E), and interior contributions, similar to what was performed in Dong et al. (2009) across 35°S. To focus on the upper layer of the ocean, we integrated the heat transport contributions from the surface to 500 m, instead of through the full ocean depth. The mean transport contribution in the west is southward (-0.59 ± 0.12 PW), and it is northward in the interior (0.74 ± 0.19 PW) and east (0.58 ± 0.16 PW). Following the same procedure described above, the phase of the CEOF1 mode with the highest correlation with MHT anomalies is calculated for each of the three areas (Figure 10). The optimal propagation phase in each area confirms the role of the CEOF1 mode in regulating the amount of heat exchanged between the tropics and extratropics. As such, stronger heat transport southward in the west and northward in the interior correspond to the CEOF1 phase with a

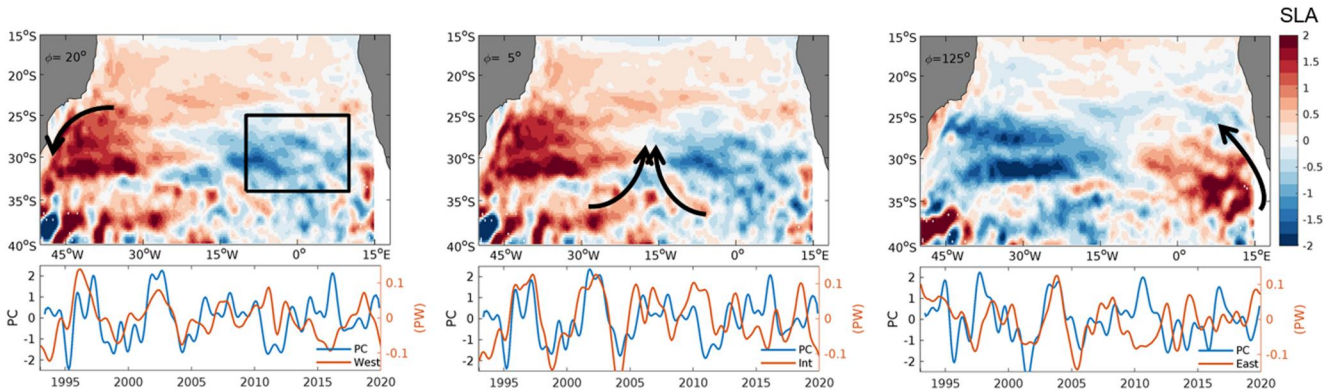

Figure 10. Same as Figure 8 but for the (a) West, (b) Interior, and (c) East components of the meridional heat transport (PW) across 30°S integrated between 0 and 500 m. The black arrows on maps show the direction of the increased geostrophic transport in each phase of the CEOF1 mode.

positive SLA in the west (Figures 10a and 10b), and an increased northward transport in the east corresponds to a CEOF1 phase with high SLA in the east (Figure 10c).

These results suggest that the 3–5 years propagation period of this mode from east to west could be modulated by and also modulate the AMOC on interannual timescales.

4. Discussion

In two recent studies, Rodrigues et al. (2019) analyzed the MHW event of 2014/2015, and Manta et al. (2018) analyzed the MHW event of 2017. Using a mixed layer heat budget methodology, they showed that surface heat flux anomalies, including increased shortwave radiation from reduced cloud cover and reduced latent heat loss from weaker winds, were responsible for the onset of marine heatwaves in the region. Both the onsets of the 2014/2015 and the 2017 MHWs were associated with the Madden-Julian oscillation (MJO) (Barreiro et al., 2019), which is the dominant mode of atmospheric variability on intraseasonal timescales in the tropics (mainly between 40 and 60 days; Madden & Julian, 1972). As the MJO propagates from the tropics, it affects convection, tropospheric winds, rainfall and surface fluxes (e.g., Matthews et al., 2004).

The role of the ocean has received much less attention than atmospheric teleconnections. Here we show that the large-scale ocean circulation (through the AMOC) is a pacemaker for the interannual occurrence of marine heatwaves in the western subtropical South Atlantic. This relationship was hypothesized here from the strong relationship between western South Atlantic temperature anomalies and sea surface height anomalies on interannual timescales. The SLA variability in the western South Atlantic is highly correlated ($r = 0.77$) with the main east-west propagating mode of SLA. The propagation of this mode agrees with the first baroclinic Rossby wave mode (Majumder et al., 2019), which is linked to the large-scale ocean adjustment. In the East, our results suggest that this mode is triggered by anomalies in the strength and location of the South Atlantic subtropical height, observed in SLP and wind composites, which can induce anomalies in coastal upwelling in the Benguela Current System region (Sun et al., 2018). SLP anomalies associated with the subtropical anticyclone have also been linked to the South Atlantic's north-south dipole of SST (Sterl & Hazeleger, 2003; Venegas et al., 1997), and our results suggest both SASD and the east-west propagating mode are related to the same forcing. The mechanism for SST propagation seems to be related to the one described in Colin de Verdière and Huck (1999) and te Raa and Dijkstra (2002), in which by crossing the South Atlantic, a warm anomaly induces southward velocity perturbations to the west and northward to the east of the center of the anomaly. This leads to a phase difference between the temperature and velocity anomalies. The perturbed velocities advect warm water southward to the west and cold water northward to the east of the initial anomaly, thereby moving the warm anomaly westward. Our results suggest that, as the mode propagates, it influences the meridional heat transport of eastern and western boundary currents and the ocean interior in different phases (Figure 10). A similar mechanism was also suggested for other western boundary currents (Elzahaby et al., 2021; Zhang et al., 2021). Because the AMOC consists of both boundary flows and ocean adjustment, this mechanism may modulate but also be influenced by AMOC variability. This relationship is supported by the significant correlation between the AMOC and the cross-basin SSH pattern (Figure 10). Therefore, this work highlights the importance of sustained AMOC monitoring for regional

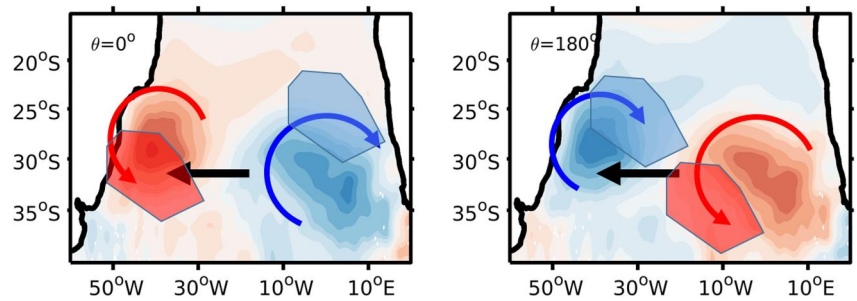

Figure 11. Schematic of the effect of the propagating oceanic heat transport on the warming and cooling of the western and eastern South Atlantic regions at two opposite phases. The contours (colored shading) are for SLA and the black horizontal arrows indicate westward propagation of the oceanic features. The red and blue arrows indicate the tendency for warming and cooling of the regions represented by the polygonal regions.

climate in the South Atlantic. The AMOC in the South Atlantic has been monitored for more than a decade by in situ observations (e.g., Dong et al., 2009; Meinen et al., 2013), and for almost three decades using satellite observations (e.g., Dong et al., 2015; Majumder et al., 2016). Previous studies have linked the AMOC to SST fingerprints in the South Atlantic (Dima & Lohmann, 2010; Lopez et al., 2016), which allows extending these time series back more than a century. Recently, Bodnariuk et al. (2021) found a link between the propagating modes in the South Atlantic and Indian and South Pacific basins, suggesting that there could be coherence of oceanic features throughout the Southern Hemisphere. Further investigations of links between the propagating SSH modes, the AMOC, and atmospheric teleconnections should be performed using numerical and simplified model studies.

5. Conclusions

The leading mode of the interannual variability of SLA in the South Atlantic is characterized by westward propagating anomalies centered at 30°S, with a periodicity of 3–5 years. The propagating SLA signals associated with this mode are positively correlated with SSTA in the western subtropical South Atlantic. The temporal phase of the propagating mode is well correlated with interannual modulations of the MHW and CS mode centered in the western South Atlantic. We estimated that there is an 82% probability that the extreme daily sea surface temperature events occur when the SLA associated with the propagating mode bears the same sign. Our analysis shows that SST modulation by SLA in the subtropical region is driven mainly by latent heat flux anomalies and by oceanic horizontal advection. The latent heat flux appears to be related to wind speed anomalies associated with the subtropical high and large-scale atmospheric waves. However, the present analysis cannot address the atmospheric mechanisms and teleconnections that influence the oceanic propagations and the large-scale heat fluxes patterns in the South Atlantic. The oceanic advection term mediates the exchange of tropical (warm) and subpolar (cold) waters in the region (Figure 11): clockwise circulation around a negative SLA anomaly favors advection of cold subpolar waters toward the subtropics, while counterclockwise circulation is generated around a positive SLA anomaly, advecting warm tropical waters into the subtropical region. The analyzed westward-propagating mode is significantly (at 90%) correlated ($r = 0.63$) with the AMOC at 30°S, and its origin in the eastern part of the basin lags the AMOC by approximately 3–9 months. Therefore, the sustained AMOC observations in the South Atlantic can provide enhanced multi-year predictability for extreme temperature events in the western side of the basin.

Data Availability Statement

Software - All calculations and figures were performed in Matlab v. 2019 (The MathWorks Inc, 2019) and Ferret v. 7.6 (Hankin et al., 1996). Ferret is a product of NOAA's Pacific Marine Environmental Laboratory. (Information is available at http://ferret.pmel.noaa.gov/Ferret/). The CEOF methodology was performed using the PCAtool v. 1.0.0.0 (Maze, 2004) toolbox in Matlab (https://www.mathworks.com/matlabcentral/fileexchange/17915-pcatool), and the Marine heatwave detection used the Zhao et al. (2019) Matlab toolbox. The mixed layer heat budget was performed using Ferret. Data - The Ssalto/Duacs altimeter SLA data (Pujol et al., 2016) was produced and distributed by the Copernicus Marine and Environment Monitoring Service (CMEMS) (https://

marine.copernicus.eu/). The OISST v.2 data (Reynolds et al., 2007) comes from the https://psl.noaa.gov/data/gridded/data.noaa.oisst.v2.highres.html. ERA5 reanalysis (Hersbach et al., 2020) was downloaded from https://cds.climate.copernicus.eu. The ORAS5 reanalysis (Zuo et al., 2018) was downloaded from https://www.ecmwf.int/en/research/climate-reanalysis/ocean-reanalysis. SeaWiFS Chl-a monthly climatology data (https://doi.org/10.5067/ORBVIEW-2/SEAWIFS/L3M/CHL/2022) are available at https://oceandata.sci.gsfc.nasa.gov/.

Acknowledgments
This research was carried out under the auspices of the Cooperative Institute for Marine and Atmospheric Studies, a cooperative institute of the University of Miami and NOAA (cooperative agreement number NA20OAR4320472). MG and DLV were supported in part by the National Oceanic and Atmospheric Administration (NOAA) Climate Variability and Predictability program (Grant NA20OAR4310407) and by the NOAA Atlantic Oceanographic and Meteorological Laboratory. The authors thank Sang-Ki Lee for comments and suggestions.

References

Amaya, D. J., Miller, A. J., Xie, S. P., & Kusaka, Y. (2020). Physical drivers of the summer 2019 North Pacific marine heatwave. *Nature Communications*, *11*(1), 1903. https://doi.org/10.1038/s41467-020-15820-w

Arthur, D., & Vassilvitskii, S. (2007). K-means++: The advantages of careful seeding. In *SODA '07: Proceedings of the eighteenth annual ACM-SIAM symposium on discrete algorithms* (pp. 1027–1035). Retrieved from https://theory.stanford.edu/sergei/papers/kMeansPP-soda.pdf

Barreiro, M., Sitz, L., de Mello, S., Franco, R. F., Renom, M., & Farneti, R. (2019). Modelling the role of Atlantic air–sea interaction in the impact of Madden–Julian Oscillation on South American climate. *International Journal of Climatology*, *39*(2), 1104–1116. https://doi.org/10.1002/joc.5865

Behrens, E., Fernandez, D., & Sutton, P. (2019). Meridional oceanic heat transport influences marine heatwaves in the Tasman Sea on interannual to decadal timescales. *Frontiers in Marine Science*, *6*, 228. https://doi.org/10.3389/fmars.2019.00228

Bodnariuk, N., Simionato, C. G., Saraceno, M., Osman, M., & Diaz, L. B. (2021). Interannual variability of the latitude of separation of the Brazil Current: Teleconnections and oceanic Rossby waves propagation. *Journal of Geophysical Research: Oceans*, *126*(10), e2021JC017557. https://doi.org/10.1029/2021JC017557

Cavole, L. M., Demko, A. M., Diner, R. E., Giddings, A., Koester, I., Pagniello, C. M. L. S., et al. (2016). Biological impacts of the 2013–2015 warm-water anomaly in the Northeast Pacific: Winners, losers, and the future. *Oceanography*, *29*(2), 273–285. https://doi.org/10.5670/oceanog.2016.32

Chang, Y., Lee, M. A., Lee, K. T., & Shao, K. T. (2013). Adaptation of fisheries and mariculture management to extreme oceanic environmental changes and climate variability in Taiwan. *Marine Policy*, *38*, 476–482. https://doi.org/10.1016/j.marpol.2012.08.002

Colin de Verdière, A., & Huck, T. (1999). Baroclinic instability: An oceanic wavemaker for interdecadal variability. *Journal of Physical Oceanography*, *29*(5), 893–910. https://doi.org/10.1175/1520-0485(1999)029<0893:biaowf>2.0.co;2

Costa, N. V., & Rodrigues, R. R. (2021). Future summer marine heatwaves in the western South Atlantic. *Geophysical Research Letters*, *48*(22), e2021GL094509. https://doi.org/10.1029/2021GL094509

Couch, C. S., Burns, J. H., Liu, G., Steward, K., Gutlay, T. N., Kenyon, J., et al. (2017). Mass coral bleaching due to unprecedented marine heatwave in Papahānaumokuākea marine national monument (Northwestern Hawaiian Islands). *PLoS One*, *12*(9), e0185121. https://doi.org/10.1371/journal.pone.0185121

Dalton, S. J., Carroll, A. G., Sampayo, E., Roff, G., Harrison, P. L., Entwistle, K., et al. (2020). Successive marine heatwaves cause disproportionate coral bleaching during a fast phase transition from El Niño to La Niña. *The Science of the Total Environment*, *715*, 136951. https://doi.org/10.1016/j.scitotenv.2020.136951

Di Lorenzo, E., & Mantua, N. (2016). Multi-year persistence of the 2014/15 North Pacific marine heatwave. *Nature Climate Change*, *6*(11), 1042–1047. https://doi.org/10.1038/nclimate3082

Dima, M., & Lohmann, G. (2010). Evidence for two distinct modes of large-scale ocean circulation changes over the last century. *Journal of Climate*, *23*(1), 5–16. https://doi.org/10.1175/2009jcli2867.1

Dong, S., Garzoli, S. L., Baringer, M. O., Meinen, C. S., & Goni, G. J. (2009). Interannual variations in the Atlantic meridional overturning circulation and its relationship with the net northward heat transport in the South Atlantic. *Geophysical Research Letters*, *36*(20), L20606. https://doi.org/10.1029/2009GL039356

Dong, S., Goni, G., & Bringas, F. (2015). Temporal variability of the South Atlantic meridional overturning circulation between 20°S and 35°S. *Geophysical Research Letters*, *42*(18), 7655–7662. https://doi.org/10.1002/2015GL065603

Dong, S., Goni, G., Domingues, R., Bringas, F., Goes, M., Christophersen, J., & Baringer, M. (2021). Synergy of in situ and satellite ocean observations in determining meridional heat transport in the Atlantic Ocean. *Journal of Geophysical Research: Oceans*, *126*(4), e2020JC017073. https://doi.org/10.1029/2020JC017073

Elzahaby, Y., Schaeffer, A., Roughan, M., & Delaux, S. (2021). Oceanic circulation drives the deepest and longest marine heatwaves in the east Australian Current System. *Geophysical Research Letters*, *48*(17), e2021GL094785. https://doi.org/10.1029/2021GL094785

Frölicher, T. L., & Laufkötter, C. (2018). Emerging risks from marine heat waves. *Nature Communications*, *9*(1), 1–4. https://doi.org/10.1038/s41467-018-03163-6

Goes, M., Christophersen, J., Dong, S., Goni, G., & Baringer, M. (2018). An updated estimate of salinity for the Atlantic Ocean sector using temperature-salinity relationships. *Journal of Oceanic and Atmospheric Technology*, *35*(9), 1771–1784. https://doi.org/10.1175/JTECH-D-18-0029.1

Goes, M., Cirano, M., Mata, M. M., & Majumder, S. (2019). Long-term monitoring of the Brazil Current transport at 22°S from XBT and altimetry data: Seasonal, interannual, and extreme variability. *Journal of Geophysical Research: Oceans*, *124*(6), 3645–3663. https://doi.org/10.1029/2018JC014809

Grodsky, S. A., & Carton, J. A. (2006). Influence of the tropics on the climate of the South Atlantic. *Geophysical Research Letters*, *33*(6), L06719. https://doi.org/10.1029/2005GL025153

Hankin, S., Harrison, D. E., Osborne, J., Davison, J., & O'Brien, K. (1996). A strategy and a tool, FERRET, for closely integrated visualization and analysis [Software]. The Journal of Visualization and Computer Animation, *7*(3), 149–157. https://doi.org/10.1002/(sici)1099-1778(199607)7:3<149::aid-vis148>3.0.co;2-x

Hersbach, H., Bell, B., Berrisford, P., Hirahara, S., Horányi, A., Muñoz-Sabater, J., et al. (2020). The ERA5 global reanalysis [Data]. Quarterly Journal of the Royal Meteorological Society, *146*(730), 1999–2049. https://doi.org/10.1002/qj.3803

Hobday, A. J., Alexander, L. V., Perkins, S. E., Smale, D. A., Straub, S. C., Oliver, E. C. J., et al. (2016). A hierarchical approach to defining marine heatwaves. *Progress in Oceanography*, *141*, 227–238. https://doi.org/10.1016/j.pocean.2015.12.014

Hobday, A. J., Oliver, E. C. J., Sen Gupta, A., Benthuysen, J. A., Burrows, M. T., Donat, M. G., et al. (2018). Categorizing and naming marine heatwaves. *Oceanography*, *31*(2), 162–173. https://doi.org/10.5670/oceanog.2018.205

Hsieh, H. J., Hsien, Y. L., Jeng, M. S., Tsai, W. S., Su, W. C., & Chen, C. A. (2008). Tropical fishes killed by the cold. *Coral Reefs*, *27*(3), 599. https://doi.org/10.1007/s00338-008-0378-3

Joh, Y., & Di Lorenzo, E. (2017). Increasing coupling between NPGO and PDO leads to prolonged marine heatwaves in the Northeast Pacific. *Geophysical Research Letters*, *44*(22), 11663–11671. https://doi.org/10.1002/2017GL075930

Le Nohaïc, M., Ross, C. L., Cornwall, C. E., Comeau, S., Lowe, R., McCulloch, M. T., & Schoepf, V. (2017). Marine heatwave causes unprecedented regional mass bleaching of thermally resistant corals in Northwestern Australia. *Scientific Reports*, *7*(1), 1–11. https://doi.org/10.1038/s41598-017-14794-y

Li, Z., Holbrook, N. J., Zhang, X., Oliver, E. C. J., & Cougnon, E. A. (2020). Remote forcing of Tasman Sea marine heatwaves. *Journal of Climate*, *33*(12), 5337–5354. https://doi.org/10.1175/JCLI-D-19-0641.1

Lopez, H., Dong, S., Lee, S.-K., & Campos, E. (2016). Remote influence of interdecadal Pacific Oscillation on the South Atlantic meridional overturning circulation variability. *Geophysical Research Letters*, *43*(15), 8250–8258. https://doi.org/10.1002/2016GL069067

Madden, R. A., & Julian, P. R. (1972). Description of global-scale circulation cells in the tropics with a 40-50 day period. *Journal of the Atmospheric Sciences*, *29*(6), 1109–1123. https://doi.org/10.1175/1520-0469(1972)029<1109:DOGSCC>2.0.CO;2

Majumder, S., Goes, M., Polito, P. S., Lumpkin, R., Schmid, C., & Lopez, H. (2019). Propagating modes of variability and their impact on the western boundary current in the South Atlantic. *Journal of Geophysical Research: Oceans*, *124*(5), 3168–3185. https://doi.org/10.1029/2018JC014812

Majumder, S., Schmid, C., & Halliwell, G. (2016). An observations and model-based analysis of meridional transports in the South Atlantic. *Journal of Geophysical Research: Oceans*, *121*(8), 5622–5638. https://doi.org/10.1002/2016JC011693

Manta, G., de Mello, S., Trinchin, R., Badagian, J., & Barreiro, M. (2018). The 2017 record marine heatwave in the Southwestern Atlantic shelf. *Geophysical Research Letters*, *45*(22), 12449–12456. https://doi.org/10.1029/2018GL081070

Matthews, A. J., Hoskins, B. J., & Masutani, M. (2004). The global response to tropical heating in the Madden–Julian oscillation during the northern winter. *Quarterly Journal of the Royal Meteorological Society*, *130*(601), 1991–2011. https://doi.org/10.1256/qj.02.123

Maze, G. (2004). PCAtool [Software]. MATLAB Central File Exchange. https://www.mathworks.com/matlabcentral/fileexchange/17915-pcatool

McEachron, L. W., Matlock, G. C., Bryan, C. E., Unger, P., Cody, T. J., & Martin, J. H. (1994). Winter mass mortality of animals in Texas bays. *Gulf of Mexico Science*, *13*(2), 6. https://doi.org/10.18785/negs.1302.06

Meinen, C., Speich, S., Perez, R. C., Dong, S., Piola, A. R., Garzoli, S. L., et al. (2013). Temporal variability of the meridional overturning circulation at 34.5°S: Results from two pilot boundary arrays in the South Atlantic. *Journal of Geophysical Research: Oceans*, *118*(12), 6461–6478. https://doi.org/10.1002/2013JC009228

Morel, A., & Antoine, D. (1994). Heating rate within the upper ocean in relation to its bio-optical state. *Journal of Physical Oceanography*, *24*(7), 1652–1665. https://doi.org/10.1175/1520-0485(1994)024<1652:hrwtuo>2.0.co;2

Morioka, Y., Tozuka, T., & Yamagata, T. (2011). On the growth and decay of the subtropical dipole mode in the South Atlantic. *Journal of Climate*, *24*(21), 5538–5554. https://doi.org/10.1175/2011jcli4010.1

Navarra, A., & Simoncini, V. (2010). Generalizations: Rotated, complex, extended and combined EOF. In *A guide to empirical orthogonal functions for climate data analysis* (pp. 69–96). Springer.

Oliver, E. C., Donat, M. G., Burrows, M. T., Moore, P. J., Smale, D. A., Alexander, L. V., et al. (2018). Longer and more frequent marine heatwaves over the past century. *Nature Communications*, *9*(1), 1324. https://doi.org/10.1038/s41467-018-03732-9

Pujol, M.-I., Faugère, Y., Taburet, G., Dupuy, S., Pelloquin, C., Ablain, M., & Picot, N. (2016). DUACS DT2014: The new multi-mission altimeter data set reprocessed over 20 years [Data]. Ocean Science, *12*(5), 1067–1090. https://doi.org/10.5194/os-12-1067-2016

Rasmusson, E., Arkin, P., Chen, W.-Y., & Jalickee, J. (1981). Biennial variations in surface temperature over the United States as revealed by singular decomposition. *Monthly Weather Review*, *109*(3), 587–598. https://doi.org/10.1175/1520-0493(1981)109<0587:bvisto>2.0.co;2

Reynolds, R. W., Smith, T. M., Liu, C., Chelton, D. B., Casey, K. S., & Schlax, M. G. (2007). Daily high-resolution-blended analyses for sea surface temperature [Data]. Journal of Climate, *20*(22), 5473–5496. https://doi.org/10.1175/2007jcli1824.1

Roberts, C. D., Calvert, D., Dunstone, N., Hermanson, L., Palmer, M. D., & Smith, D. (2016). On the drivers and predictability of seasonal-to-interannual variations in regional sea level. *Journal of Climate*, *29*(21), 7565–7585. https://doi.org/10.1175/jcli-d-15-0886.1

Rodrigues, R. R., Taschetto, A. S., Gupta, A. S., & Foltz, G. R. (2019). Common cause for severe droughts in South America and marine heatwaves in the South Atlantic. *Nature Geoscience*, *12*(8), 620–626. https://doi.org/10.1038/s41561-019-0393-8

Santos, R. O., Rehage, J. S., Boucek, R., & Osborne, J. (2016). Shift in recreational fishing catches as a function of an extreme cold event. *Ecosphere*, *7*(6), e01335. https://doi.org/10.1002/ecs2.1335

Sen Gupta, A., Thomsen, M., Benthuysen, J. A., Hobday, A. J., Oliver, E., Alexander, L. V., et al. (2020). Drivers and impacts of the most extreme marine heatwave events. *Scientific Reports*, *10*(1), 1–15. https://doi.org/10.1038/s41598-020-75445-3

Smale, D. A., Wernberg, T., Oliver, E. C. J., Thomsen, M., Harvey, B. P., Straub, S. C., et al. (2019). Marine heatwaves threaten global biodiversity and the provision of ecosystem services. *Nature Climate Change*, *9*(4), 306–312. https://doi.org/10.1038/s41558-019-0412-1

Sterl, A., & Hazeleger, W. (2003). Coupled variability and air-sea interaction in the South Atlantic Ocean. *Climate Dynamics*, *21*(7–8), 559–571. https://doi.org/10.1007/s00382-003-0348-y

Stevenson, J. W., & Niiler, P. P. (1983). Upper ocean heat budget during the Hawaii-to-Tahiti shuttle experiment. *Journal of Physical Oceanography*, *13*(10), 1894–1907. https://doi.org/10.1175/1520-0485(1983)013<1894:UOHBDT>2.0.CO;2

Stuart-Smith, R. D., Brown, C. J., Ceccarelli, D. M., & Edgar, G. J. (2018). Ecosystem restructuring along the Great Barrier Reef following mass coral bleaching. *Nature*, *560*(7716), 92–96. https://doi.org/10.1038/s41586-018-0359-9

Sun, X., Vizy, E. K., & Cook, K. H. (2018). Land–atmosphere–ocean interactions in the southeastern Atlantic: Interannual variability. *Climate Dynamics*, *52*(1–2), 539–561. https://doi.org/10.1007/s00382-018-4155-x

Sweeney, C., Gnanadesikan, A., Griffies, S. M., Harrison, M. J., Rosati, A. J., & Samuels, B. L. (2005). Impacts of shortwave penetration depth on large-scale ocean circulation and heat transport. *Journal of Physical Oceanography*, *35*(6), 1103–1119. https://doi.org/10.1175/jpo2740.1

Taburet, G., Sanchez-Roman, A., Ballarotta, M., Pujol, M. I., Legeais, J. F., Fournier, F., et al. (2019). DUACS DT2018: 25 years of reprocessed sea level altimetry products. *Ocean Science*, *15*(5), 1207–1224. https://doi.org/10.5194/os-15-1207-2019

te Raa, L. A., & Dijkstra, H. A. (2002). Instability of the thermohaline ocean circulation on interdecadal timescales. *Journal of Physical Oceanography*, *32*(1), 138–160. https://doi.org/10.1175/1520-0485(2002)032<0138:iottoc>2.0.co;2

The MathWorks Inc. (2019). MATLAB version: 9.6.0.1135713 update 3 (R2019a) [Software]. The MathWorks Inc. Retrieved from https://www.mathworks.com

Venegas, S. A., Mysak, L. A., & Straub, D. N. (1997). Atmosphere–Ocean coupled variability in the South Atlantic. *Journal of Climate*, *10*(11), 2904–2920. https://doi.org/10.1175/1520-0442(1997)010<2904:AOCVIT>2.0.CO;2

Vialard, J., Menkes, C., Boulanger, J., Delecluse, P., Guilyardi, E., McPhaden, M. J., & Madec, G. (2001). A model study of oceanic mechanisms affecting equatorial Pacific Sea surface temperature during the 1997–98 El Niño. *Journal of Physical Oceanography*, *31*(7), 1649–1675. https://doi.org/10.1175/1520-0485(2001)031<1649:amsoom>2.0.co;2

Volkov, D. L., Lee, S.-K., Domingues, R., Zhang, H., & Goes, M. (2019). Interannual sea level variability along the southeastern seaboard of the United States in relation to the gyre-scale heat divergence in the North Atlantic. *Geophysical Research Letters*, *46*(13), 7481–7490. https://doi.org/10.1029/2019GL083596

Wainer, I., Prado, L. F., Khodri, M., & Otto-Bliesner, B. (2014). Reconstruction of the South Atlantic Subtropical Dipole index for the past 12,000 years from surface temperature proxy. *Scientific Reports*, *4*(1), 1–8. https://doi.org/10.1038/srep05291

Wheeler, P. A., Huyer, A., & Fleischbein, J. (2003). Cold halocline, increased nutrients and higher chlorophyll off Oregon in 2002. *Geophysical Research Letters*, *30*(15), 8021. https://doi.org/10.1029/2003gl017395

Woodhead, P. M. (1964). The death of North Sea fish during the winter of 1962/63, particularly with reference to the sole, Solea vulgaris. *Helgoländer Wissenschaftliche Meeresuntersuchungen*, *10*(1–4), 283–300. https://doi.org/10.1007/bf01626114

Zapata, F. A., Jaramillo-González, J., & Navas-Camacho, R. (2011). Extensive bleaching of the coral Porites lobata at Malpelo Island, Colombia, during a cold water episode in 2009. *Boletín de Investigaciones Marinas y Costeras-INVEMAR*, *40*, 185–193.

Zhang, Y., Du, Y., Feng, M., & Hu, S. (2021). Long-lasting marine heatwaves investigated by ocean planetary waves in the tropical Indian Ocean during 2015–2016 and 2019–2020. *Geophysical Research Letters*, *48*(21), e2021GL095350. https://doi.org/10.1029/2021gl095350

Zhao, Z., & Marin, M. (2019). A MATLAB toolbox to detect and analyze marine heatwaves [Software]. Journal of Open Source Software, *4*(33), 1124. https://doi.org/10.21105/joss.01124

Zuo, H., Balmaseda, M. A., Tietsche, S., Mogensen, K., & Mayer, M. (2018). The ECMWF operational ensemble reanalysis-analysis system for ocean and sea-ice: A description of the system and assessment [Data]. Ocean Science Discussions, *15*(3), 779–808. https://doi.org/10.5194/os-15-779-2019